The unexpected diversity of dwarf galaxy rotation curves

Kyle A. Oman,[1]* Julio F. Navarro,[1]† Azadeh Fattahi,[1] Carlos S. Frenk,[2] Till Sawala,[2] Simon D. M. White,[3] Richard Bower,[2] Robert A. Crain,[4] Michelle Furlong,[2] Matthieu Schaller,[2] Joop Schaye[5] and Tom Theuns[2]

[1]*Department of Physics & Astronomy, University of Victoria, Victoria, BC V8P 5C2, Canada*
[2]*Institute for Computational Cosmology, Department of Physics, University of Durham, South Road, Durham DH1 3LE, UK*
[3]*Max-Planck Institute for Astrophysics, D-85748 Garching, Germany*
[4]*Astrophysics Research Institute, Liverpool John Moores University, IC2, Liverpool Science Park, 146 Brownlow Hill, Liverpool L3 5RF, UK*
[5]*Leiden Observatory, Leiden University, PO Box 9513, NL-2300 RA Leiden, the Netherlands*

ABSTRACT

We examine the circular velocity profiles of galaxies in Λ cold dark matter (CDM) cosmological hydrodynamical simulations from the EAGLE and LOCAL GROUPS projects and compare them with a compilation of observed rotation curves of galaxies spanning a wide range in mass. The shape of the circular velocity profiles of simulated galaxies varies systematically as a function of galaxy mass, but shows remarkably little variation at fixed maximum circular velocity. This is especially true for low-mass dark-matter-dominated systems, reflecting the expected similarity of the underlying CDM haloes. This is at odds with observed dwarf galaxies, which show a large diversity of rotation curve shapes, even at fixed maximum rotation speed. Some dwarfs have rotation curves that agree well with simulations, others do not. The latter are systems where the inferred mass enclosed in the inner regions is much lower than expected for CDM haloes and include many galaxies where previous work claims the presence of a constant density 'core'. The 'cusp versus core' issue is thus better characterized as an 'inner mass deficit' problem than as a density slope mismatch. For several galaxies, the magnitude of this inner mass deficit is well in excess of that reported in recent simulations where cores result from baryon-induced fluctuations in the gravitational potential. We conclude that one or more of the following statements must be true: (i) the dark matter is more complex than envisaged by any current model; (ii) current simulations fail to reproduce the diversity in the effects of baryons on the inner regions of dwarf galaxies; and/or (iii) the mass profiles of 'inner mass deficit' galaxies inferred from kinematic data are incorrect.

Key words: galaxies: haloes – galaxies: structure – dark matter.

1 INTRODUCTION

Cosmological simulations have led to a detailed theoretical characterization of the clustering of dark matter on galaxy scales. It is now well established that, when baryons may be neglected, the equilibrium mass profiles of cold dark matter (CDM) haloes are approximately self-similar and can be adequately approximated by a simple formula (Navarro, Frenk & White 1996, 1997). The 'NFW profile', as this is commonly known, has a formally divergent density 'cusp' near the centre, $\rho \propto r^{-\gamma}$, with $\gamma = 1$, and steepens gradually at larger radii. The corresponding circular velocity profile, $V_{\rm circ}(r)$, is thus relatively steep near the centre, $V_{\rm circ} \propto r^{1/2}$, in contrast with the rotation curves of some dwarf galaxies, where the inner rota-

tion speed rises linearly with radius. The latter behaviour suggests that the dark matter density profile has a shallower inner slope than predicted by simulations, closer to a constant density 'core' rather than a steeply divergent 'cusp'. This 'cusp versus core' problem (Flores & Primack 1994; Moore 1994) has been known since the mid-1990s and has elicited a number of proposed solutions.

One is that the dark matter is not 'cold'. Cores can be produced in dark matter haloes by particle physics effects if the dark matter particles have specific properties that differ from those of weakly interacting massive particles or axions, the standard CDM candidates. For example, phase space constraints give rise to cores in warm dark matter (WDM) haloes (e.g. Bode, Ostriker & Turok 2001; Lovell et al. 2012), although current lower limits on WDM particle masses imply cores that are much smaller than those inferred for many dwarfs (Macciò et al. 2012a; Shao et al. 2013; Viel et al. 2013).

Alternatively, elastic collisions between particles of self-interacting dark matter (SIDM; see e.g. Spergel & Steinhardt 2000) may create cores, provided the cross-sections are the right size. SIDM has fallen somewhat out of favour because of concerns that it may fail to account for the central dark matter density profiles of galaxy clusters (Miralda-Escudé 2002) or that it would lead to the dissolution of individual galaxies in clusters (Gnedin & Ostriker 2001). However, recent work has concluded that those arguments may be countered by appealing to velocity-dependent cross-sections (Vogelsberger, Zavala & Loeb 2012) or by re-evaluating carefully the observational constraints. Indeed, Rocha et al. (2013) argue that a velocity-independent specific cross-section of the order of $\sigma/m \sim 0.1$ cm^2 g^{-1} can reproduce simultaneously dwarf and cluster observations, although this conclusion relies on a relatively uncertain extrapolation of their results to the regime of dwarfs. As a result, the situation remains unsettled. Zavala, Vogelsberger & Walker (2013), for example, have recently argued that only a finely tuned SIDM model can be reconciled with observation while Elbert et al. (2014) have concluded the opposite, although we note that the latter work is based on resimulations of only two haloes of similar (~ 40 km s^{-1}) circular velocity.

An alternative is that rotation curves may be reconciled with ΛCDM haloes by 'baryon effects' operating during the formation of a galaxy (Navarro, Eke & Frenk 1996; Gnedin & Zhao 2002; Read & Gilmore 2005). In particular, recent simulations in which star formation occurs in a series of short bursts where dense clouds of gas are continually assembled and violently dispersed have been shown to drive potential fluctuations that can induce constant density cores at the centre of ΛCDM haloes (Mashchenko, Couchman & Wadsley 2006; Governato et al. 2010, 2012; Brook et al. 2012; Teyssier et al. 2013; Madau, Shen & Governato 2014). Although there is no consensus that galaxy formation necessarily has this effect (other simulations make realistic galaxies without producing cores; see e.g. Schaller et al. 2015, and our discussion below), there is growing consensus that the inner dark matter profiles can, in principle, be reshaped during the formation of a galaxy, even a dark-matter-dominated one, in a manner that may depend on its merger history (see e.g. Di Cintio et al. 2014; Oñorbe et al. 2015). 'Baryon-induced' cores in CDM haloes would be difficult to distinguish from those produced by other effects, such as collisional effects in the case of SIDM (see e.g. Vogelsberger et al. 2014b; Bastidas Fry et al. 2015), complicating matters further.

Finally, it has been argued that a critical reappraisal of the actual constraints placed on the inner dark matter density slope by observations might be needed, citing concerns about complexities such as non-circular motions (Swaters et al. 2003), instrumental smearing effects (van den Bosch et al. 2000; Swaters et al. 2003), and/or departures from axisymmetry (Hayashi et al. 2004), all of which may complicate the relation between the observational data and the underlying gravitational potential. The advent of two-dimensional observational surveys with better sensitivity and angular resolution have allayed some of these earlier concerns (e.g. Simon et al. 2003; de Blok et al. 2008; Kuzio de Naray, McGaugh & de Blok 2008; Oh et al. 2011, 2015; Adams et al. 2014), and have led to the view that reliable determination of the inner slope of the dark matter density profile is indeed possible.

Some questions, however, remain. Adams et al. (2014), for example, report inner slopes as steep as $\gamma = 0.67 \pm 0.10$ for a sample of seven nearby dwarfs, whereas Oh et al. (2011) report much shallower slopes ($\gamma = 0.29 \pm 0.07$) for seven dwarfs selected from the THINGS survey (Walter et al. 2008). Whether these discrepancies reflect a genuine physical difference between the galaxies in each
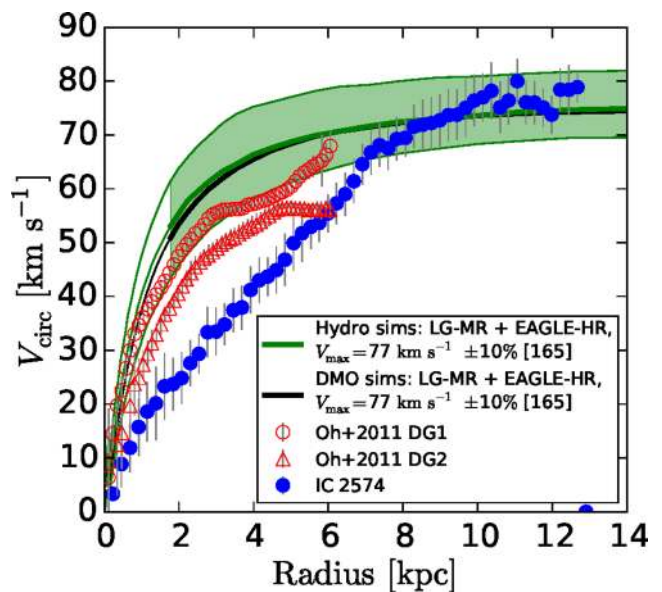

Figure 1. Rotation curves of IC 2574 (filled circles) and of the simulated galaxies DG1 (open circles) and DG2 (open triangles), taken from Oh et al. (2011). The green line shows the median circular velocity curve of all galaxies from our LG-MR and EAGLE-HR simulations (see Section 2.1) with $V_{\mathrm{max}} = 77$ km s^{-1} $\pm$ 10 per cent, matching the value of V_{max} of IC 2574. The shaded area indicates the 10th–90th percentile range at each radius. The lines become thinner and the shading stops inside the average convergence radius, computed following the prescription of Power et al. (2003). The numbers in square brackets in the legend are the numbers of galaxies/haloes that contribute to that velocity bin. The solid black line is the median circular velocity profile of haloes of the same V_{max}, identified in our DMO simulations.

of those samples, or a systematic difference in the modelling of the observational data, is still unclear. What is clear is that the inferred slopes are highly sensitive to how the mass of the baryonic population is modelled as well as to how the inevitable presence of non-circular motions near the centre is accounted for.

The case of NGC 2976 offers a sobering example: when inner kinematic peculiarities in the gas are ignored a nearly constant density core is inferred (Simon et al. 2003), while a much steeper slope is inferred from Jeans modelling of stellar tracers (Adams et al. 2012). Although the disagreement can be resolved once the non-circular motions are accounted for and the total mass of the stellar component is better constrained (Adams et al. 2014), this example illustrates the difficulty of inferring γ, even when quality multitracer data at high resolution are available.

A further drawback of focusing the discussion on the central value of γ is that it risks missing an important dimension of the problem, which concerns the total mass enclosed within the inner regions of a galaxy. This may be illustrated by the case of IC 2574, one of seven systems whose rotation curves were compared by Oh et al. (2011) to simulated galaxies where baryon-induced fluctuations had flattened the dark matter cusp (Governato et al. 2010). Oh et al. (2011) conclude that the simulated galaxies have 'haloes with a central mass distribution similar to that observed in nearby dwarf galaxies', a conclusion based on the similarity of the innermost values of γ.

Although the value of γ in the inner $\sim$1 kpc of these systems might be similar, the full circular velocity profiles of IC 2574 and simulated galaxies are actually very different. We show this in Fig. 1, where we plot the circular velocity profile of IC 2574 (filled circles)

with that of DG1 (open circles) and DG2 (open triangles), the two simulated galaxies from the Oh et al. (2011) study. The simulated galaxies show a clear excess of mass in the inner regions compared to IC 2574, despite the 'cores' in the dark matter carved out by baryons. The reason for the discrepancy is that these cores are small, and only affect the inner kpc, whereas IC 2574 shows a linearly rising rotation curve out to ∼8 kpc. The 'baryon-induced' cores in these simulations are clearly too small to reconcile CDM with rotation curves of galaxies like IC 2574, so the reported agreement between observation and simulation is, in this case, illusory.

The above discussion demonstrates that resolving the 'cusp versus core' problem requires more than just matching the innermost values of γ. Even if baryon effects are able to flatten the innermost value of γ to values consistent with observed estimates (see e.g. fig. 2 in Pontzen & Governato 2014, for a comparison at 500 pc from the centre), this is not enough to ensure that simulated rotation curves agree with observation. We argue therefore for a reassessment of the 'cusp versus core' controversy where full circular velocity profiles of observed galaxies are directly compared with the results of cosmological hydrodynamical simulations. This has only become possible very recently, given the advent of cosmological hydrodynamical simulations able to produce a realistic galaxy population and, presumably, also realistic rotation curves (see e.g. Vogelsberger et al. 2014a; Schaye et al. 2015).

The analysis we advocate here, which extends to lower masses that of Schaller et al. (2015), has a number of advantages. One is that the inner regions, which are difficult to observe *and* to simulate, are less emphasized in the comparison. The second is that it makes full use of the predictive power of the ΛCDM paradigm. Earlier work had left considerable room for discussion because of uncertainties, for example, in the normalization of the NFW mass–concentration relation, which determines the actual density profile of a halo of given mass. That debate has now been settled: the cosmological parameters are known to exquisite accuracy (see e.g. Planck Collaboration XIII 2015), and large cosmological simulations with excellent resolution have characterized conclusively the mass–concentration relation, its normalization, and scatter (see e.g. Neto et al. 2007; Duffy et al. 2008; Macciò, Dutton & van den Bosch 2008; Zhao et al. 2009; Prada et al. 2012; Ludlow et al. 2014). As a result, simulated galaxies can now be compared directly with observations without need for rescalings or other adjustments.

We adopt this view here by considering the circular velocity profiles of galaxies selected from the EAGLE and LOCAL GROUPS (LG)[1] simulation projects. The simulated galaxies cover a wide range of maximum circular velocity, from 25 to 250 km s^{-1}, and are compared with data compiled from the literature for galaxies that span a similar range in maximum rotation velocity. We begin by presenting the simulated curves in Section 2 and the observed compilation in Section 3. We then compare them and discuss our results in Section 4, before summarizing our main conclusions in Section 5.

2 CIRCULAR VELOCITY PROFILES OF SIMULATED GALAXIES

We discuss here the circular velocity curves of galaxies selected from the EAGLE (Crain et al. 2015; Schaye et al. 2015) and LG (Sawala et al. 2015) simulation projects. EAGLE is calibrated to reproduce, in a cosmological volume, the observed population of

Table 1. Summary of the key parameters of the EAGLE and LG simulations used in this work. Details of the cosmological parameters are available in Komatsu et al. (2011, *WMAP*7) and Planck Collaboration XVI (2014, Planck13).

| Simulation | Particle masses (M$_{\odot}$) | | Max softening length (pc) | Cosmology |
	DM	Gas		
EAGLE-HR	1.2×10^6	2.3×10^5	350	*Planck*13
LG-LR	7.3×10^6	1.5×10^6	712	*WMAP*7
LG-MR	5.9×10^5	1.3×10^5	308	*WMAP*7
LG-HR	5.0×10^4	1.0×10^4	134	*WMAP*7

galaxies, including their abundance as a function of galaxy mass and their typical size. LG simulates volumes tailored to match the Local Group environment with the same physics as EAGLE but at higher numerical resolution. We refer the interested reader to the above references for details, and provide here only a brief summary of the parameters most relevant to our analysis.

2.1 The numerical simulations

2.1.1 The EAGLE simulations

The EAGLE project is a suite of cosmological hydrodynamical simulations run with a substantially modified version of the P-GADGET3 code, itself a descendent of the publicly available GADGET2 (Springel 2005). In this work, we use only the highest resolution realization in the suite, which we denote EAGLE-HR (Ref-L025N0752[2] in the nomenclature of Schaye et al. 2015). This simulation has a cube side length of 25 comoving Mpc; 752^3 dark matter particles each of mass 1.21×10^6 M$_{\odot}$; the same number of gas particles each of mass 2.26×10^5 M$_{\odot}$; and a Plummer-equivalent gravitational softening length of 350 proper pc (switching to comoving above redshift 2.8). The cosmology adopted is that of the Planck Collaboration XVI (2014), with $\Omega_m = 0.307$, $\Omega_\Lambda = 0.693$, $\Omega_b = 0.04825$, $h = 0.6777$ and $\sigma_8 = 0.8288$. EAGLE uses the pressure-entropy formulation of smoothed particle hydrodynamics (Hopkins 2013), and includes subgrid models for radiative cooling, star formation, stellar and chemical enrichment, energetic stellar feedback, black hole accretion and mergers, and AGN feedback.

2.1.2 The LG simulations

The LG project is a suite of zoom-in hydrodynamical simulations of regions selected from cosmological dark-matter-only (DMO) simulations to contain two haloes with approximately the masses and dynamics of the Milky Way and M31, and no other nearby large structures (Fattahi et al., in preparation). LG uses the same code and physics as the 'Ref' EAGLE simulations. The same volumes are simulated at three different resolution levels, which we denote LG-LR, LG-MR and LG-HR for low, medium and high resolution, respectively. Each resolution level is separated by a factor of ∼10 in particle mass and a factor of ∼2 in force resolution.

Table 1 summarizes the particle masses and softening lengths of each resolution level. We note that the LG-MR resolution level corresponds closely to EAGLE-HR. There are 12 volumes, all of which have been simulated at LG-LR and LG-MR resolution levels.

---

[1] The LOCAL GROUPS project is the former name of the APOSTLE project. The new name was chosen as this article went to press.

[2] Though the fiducial EAGLE model for this box size and resolution is Recal-L025N0752, we use the Ref-L025N0752 model because it more closely matches the subgrid physics used in the LG simulations.
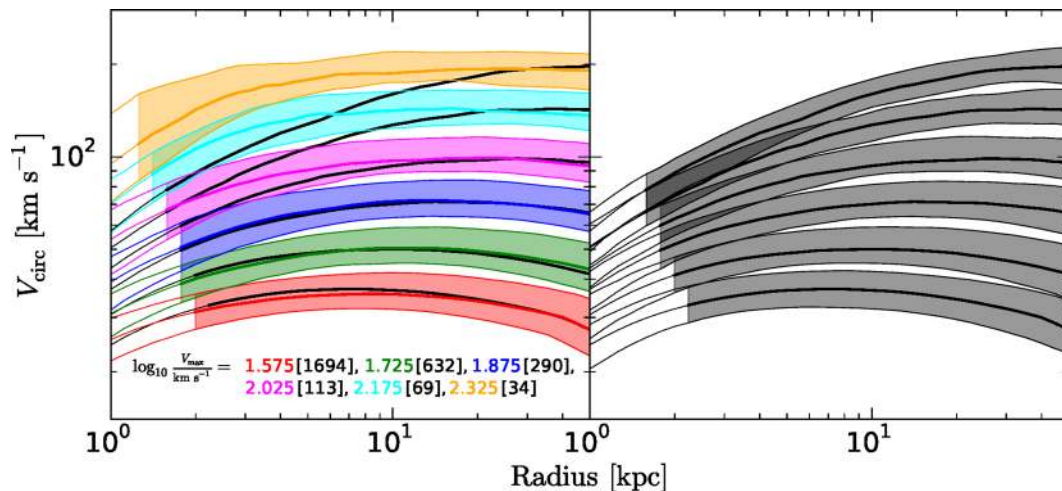
Figure 2. Circular velocity curves of simulated galaxies in the EAGLE-HR and LG-MR simulations, which have similar mass and force resolution. The left-hand panel shows the results for hydrodynamical simulations; the right-hand panel shows results for the corresponding DMO runs. Systems are grouped according to their maximum circular velocity in bins of 0.15-dex width as listed in the legend. The number of systems in each bin is also listed in the legend, in square brackets. Solid curves indicate the median circular velocity curve for galaxies in each bin; the shaded areas show the 10th–90th percentile range. The curves become thinner and shading stops inside the average convergence radius, computed for each bin using the prescription of Power et al. (2003). The solid black curves are the same in both panels, and indicate the median circular velocity curves in the DMO simulations.

Only volumes 1 and 4 have been simulated at high resolution. For each hydrodynamical simulation there is also a corresponding DMO simulation of the same region at the same resolution. The *WMAP*7 cosmological parameters (Komatsu et al. 2011) are used in LG,[3] with $\Omega_m = 0.2727$, $\Omega_\Lambda = 0.728$, $\Omega_b = 0.04557$, $h = 0.702$ and $\sigma_8 = 0.807$.

The LG simulation suite produces realistic Local Group-like environments, reproducing the stellar mass function of Milky Way and M31 satellites, and that of Local Group dwarf galaxies (Sawala et al. 2014) using the same calibration parameter choices as the EAGLE-Ref simulations.

2.1.3 Halo finding

Structures are identified in our simulations using the SUBFIND algorithm (Springel et al. 2001; Dolag et al. 2009). Particles are first grouped into friends-of-friends (FoF) haloes by linking together dark matter particles separated by less than 0.2 times the mean interparticle spacing; gas and star particles are assigned to the same FoF halo as their nearest dark matter particle. Substructures are then separated along saddle points in the density distribution; in this step dark matter, gas and star particles are treated as a single distribution of mass. Finally, particles that are not gravitationally bound to the substructures are removed. The result is a collection of substructures termed 'subhaloes', each typically corresponding to a single galaxy.

2.2 Circular velocity curves

The circular velocity profiles of simulated galaxies, $V_{circ}(r) = (GM(<r)/r)^{1/2}$, where $M(<r)$ is the mass enclosed within radius r, are shown in the left-hand panel of Fig. 2. Here, we have gathered all 'central' galaxies (i.e. excluding satellites)

in the 12 LG-MR simulations, together with all centrals in the EAGLE-HR simulation, and binned them according to their maximum circular velocity, V_{max}. We adopted bins of 0.15-dex width, centred at $\log_{10}(V_{max}/\mathrm{km\ s^{-1}}) = 1.575$, 1.725, 1.875, 2.025, 2.175, 2.325, and show the median rotation curve for galaxies in each bin with solid lines. The shaded areas indicate, at each radius, the 10th and 90th percentile velocity for all galaxies in each bin. The number of galaxies in each bin is listed in the legend.

This figure illustrates two important points. One is that the shapes of the circular velocity curves of ΛCDM galaxies are a strong function of the maximum circular velocity of the system. Indeed, once V_{max} is specified, the circular velocity profile of a system is very well constrained at all radii that are resolved[4] by the simulations. The second point is that, in general, circular velocity curves of systems with substantially different V_{max} do not cross, so that in principle a well measured circular velocity at almost any radius may be translated into an excellent constraint on V_{max}.

These characteristics of the circular velocity curves are largely a reflection of the self-similar nature of ΛCDM haloes, modified by the baryonic component. This may be seen in the right-hand panel of Fig. 2, which is analogous to that in the left, but for systems identified in DMO simulations of the same EAGLE and LG volumes. (The solid black lines are the same in both panels and indicate the median rotation curves in the DMO simulations.) As discussed by Schaller et al. (2015), the effects of baryons are mainly discernible in systems with $V_{max} > 60\ \mathrm{km\ s^{-1}}$. In those systems, the assembly of the baryonic component of the galaxy leads to an increase in mass that tends to flatten the $V_{circ}(r)$ profile in the inner few kpc.

In systems with $V_{max} < 60\ \mathrm{km\ s^{-1}}$, on the other hand, the galaxy formation 'efficiency' is very low, and the baryonic mass of the central galaxy has, in general, a negligible effect on the circular velocity curve, even in the inner regions. Our simulations thus show

---

[3] The differences between the cosmological parameters used in the EAGLE and LG projects are very small and of little consequence to this study.

[4] We adopt in all cases the 'convergence radius' introduced by Power et al. (2003), as computed from the DMO simulations. This radius marks the point where curves turn thinner and the shading stops in all figures.

little evidence for the formation of a constant-density 'core' near the centre of dwarf galaxies, suggesting that the dark matter 'core creation' mechanism discussed by Pontzen & Governato (2014) is not a general result of ΛCDM simulations that produce realistic galaxy populations, but rather a consequence of particular algorithmic choices adopted to simulate star formation and feedback.

Indeed, simulations that produce 'cores' generally adopt a high-density threshold for star formation ($n_H \gtrsim 100 \, \mathrm{cm}^{-3}$; e.g. Governato et al. 2010) that results in micro bursts of star formation concentrated in highly compact gas clouds that can be rapidly dispersed by feedback. This mode of star formation is not present in our simulations, which adopt a lower effective star formation threshold ($n_H \gtrsim 0.1 \, \mathrm{cm}^{-3}(Z/0.002)^{-0.64}$, depending on the metallicity Z and motivated by models of the H I–H$_2$ transition; Schaye 2004) because we do not attempt to model a cold ($T \ll 10^4$ K) interstellar gas phase. Our simulations thus allow star formation to occur throughout the rotationally supported gaseous disc of a galaxy, limiting the sudden fluctuations in the gravitational potential on small scales.

Although we do not see obvious evidence for constant density cores in the circular velocity profiles, we do find ~1 kpc cores in the dark matter density profile of some galaxies with $V_{\mathrm{max}} \gtrsim 100 \, \mathrm{km \, s}^{-1}$. These cores are *only* present in the dark matter – any dark mass displaced is actually replaced by baryons so that the net result is typically an overall increase in the total mass in the inner regions and a steepening of the potential. As a result, these cores cannot explain the linearly rising rotation curves of dwarf galaxies, and are of little consequence to the rest of our analysis.

Fig. 3 offers evidence that the lack of 'cores' in the *total* mass profiles in our simulations is not a result of insufficient numerical resolution. Here we show, in linear units, the circular velocity profiles of LG galaxies in two bins of V_{max}, simulated at three different numerical resolutions (LG-HR, LG-MR, and LG-LR; see Section 2.1.2). As in Fig. 2, the shaded regions in Fig. 3 show the 10th–90th percentile range spanned by the $V_{\mathrm{circ}}(r)$ curves in each bin, for the medium-resolution (MR) and low-resolution (LR) simulations. The thin lines in Fig. 3 correspond to individual systems identified in the high-resolution (HR) version of the same simulations. Fig. 3 shows that, at all well-resolved radii, the circular velocity profiles are insensitive to numerical resolution, despite the fact that the LG simulation series span a factor of $12^2 = 144$ in particle mass and of more than ~5 in force resolution.

We emphasize that, although our simulations do not form 'cores', they do produce galaxies whose abundance, structural properties, and evolution seem in good accord with observational constraints (see e.g. Sawala et al. 2014; Schaller et al. 2015; Furlong et al. 2015; Schaye et al. 2015). The formation of dark matter 'cores' thus does not appear to be a requisite ingredient of galaxy formation simulations that successfully reproduce the structural properties of the observed galaxy population, at least for galaxies with stellar masses $M_* \gtrsim 10^9 \, \mathrm{M}_\odot$.

3 OBSERVED ROTATION CURVES

Our sample of galaxy rotation curves is compiled from several literature sources. We describe the sources of our compilation in detail in the appendix, and list some key properties of the individual rotation curves that we use in our analysis in Table A1. Our compilation retains only recent data sets (i.e. published after 2001), and favours, where possible, data sets based on two-dimensional velocity fields, such as the integral-field optical data sets of Kuzio de Naray et al. (2008); or the high-resolution H I data cubes from Oh et al. (2015).
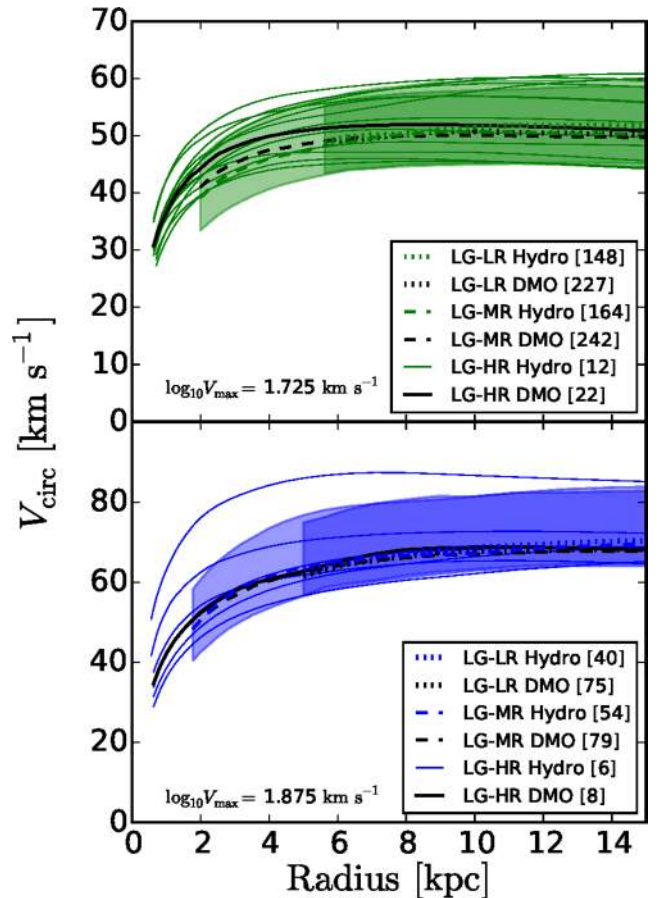

Figure 3. As Fig. 2, but for only two velocity bins, and shown in linear units. The total number of galaxies in each bin are listed in the legend. The dotted lines correspond to galaxies in the low-resolution LG-LR simulations, shown only down to their convergence radii. The dashed line shows the same, but for galaxies in the medium resolution LG-MR simulations. Thin solid curves correspond to individual systems in the high-resolution LG-HR simulations. Only 2 of the 12 LG volumes have been simulated at high resolution, hence the relatively small number of individual curves in each panel. The black lines show the median circular velocity profile for DMO simulations.

For more massive galaxies, we supplement our compilation with the long-slit rotation curves of Reyes et al. (2011)[5] and Kauffmann et al. (2015). Although our data set is by no means complete, it contains 304 rotation curves (and an additional 189 from Reyes et al. 2011) spanning a wide range of V_{max}, from 21 to 350 km s^{-1}. It also contains the majority of the dwarf galaxies that have been used in the literature to illustrate the 'cusp versus core' problem.

We assume throughout our analysis that the published rotation curves (which have been corrected, in most cases, for inclination effects, asymmetric drift, and non-circular motions) provide a fair approximation to the circular velocity profiles of galaxies in our sample and hereafter refer to both as 'V_{circ}'. We note that this is a strong assumption which may fail for a number of dwarf systems where the observed galaxy is clearly highly irregular.

---

[5] Full rotation curves were not available, we use instead the published parameters of fits to their rotation curves.
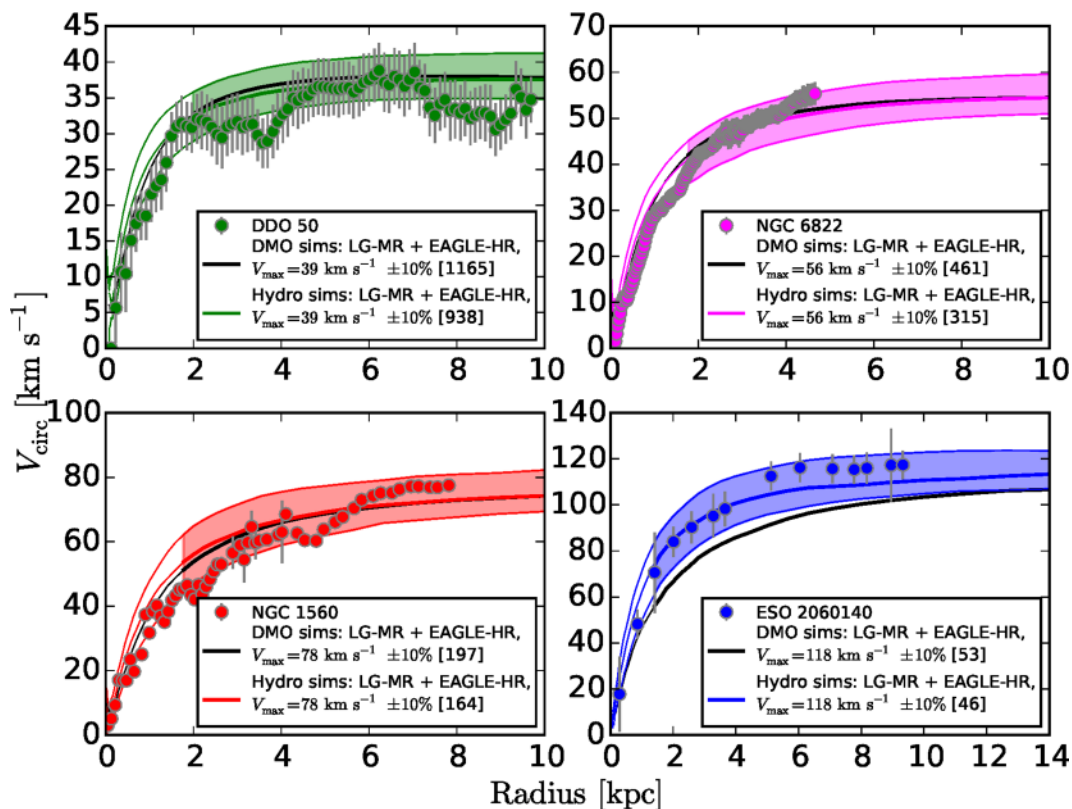
Figure 4. Four examples of galaxies in our sample with rotation curves that are in good agreement with the circular velocity curves of our ΛCDM hydrodynamical simulations. The four galaxies have been chosen to span a wide range in maximum circular velocity, from ~30 (top left) to ~120 km s^{-1} (bottom right). As in Fig. 2, the solid curves and shaded areas show the median (and 10th–90th percentile range) of all simulated galaxies in 20 per cent-width bins centred at the maximum circular velocity of the galaxy in each panel (see legend). The solid black curve corresponds to the median circular velocity curve of our DMO simulations.

4 OBSERVED VERSUS SIMULATED ROTATION CURVES

4.1 The similarity of simulated circular velocity curves

The general properties of the rotation curves of simulated galaxies shown in Fig. 2 are in reasonable agreement with those of observed galaxies, thus extending the agreement between EAGLE and observations noted by Schaller et al. (2015, e.g. their fig. 6) for $V_{max} > 100$ km s^{-1} to lower mass systems. Circular velocities tend to rise sharply and stay flat in massive galaxies, but to rise more slowly in dwarf systems, where baryons play a less important role.

The agreement is not just qualitative. This may be seen in Fig. 4, where we compare directly the rotation curves of four galaxies of different circular velocity with the simulation results. The comparison is made with simulated systems whose maximum circular velocity matches, within 10 per cent, that of the observed galaxy, without any rescaling. The match in V_{max} ensures as well that the baryonic masses of simulated and observed galaxies are comparable, since the simulated systems satisfy the observed baryonic Tully–Fisher relation (Sales et al., in preparation).

The excellent agreement shown in Fig. 4 is meant to illustrate a more general point: the rotation curves of *many* galaxies, dwarfs included, are actually consistent with ΛCDM predictions. This is important to emphasize, since it is often thought that ΛCDM rotation curves are in conflict with data for *all* or *a majority* of galaxies, especially dwarfs.

4.2 The diversity of observed rotation curves

Actually, the main difference between simulated and observed rotation curves is the great *diversity* of the latter (especially for dwarfs), which is unexpected according to our results. We illustrate this in Fig. 5, where the rotation curves of four different dwarf galaxies of similar maximum circular velocity are compared with simulated galaxies of matching V_{max}.

The four galaxies in this figure have been selected to illustrate the large diversity of rotation curve shapes at fixed V_{max}. According to the baryonic Tully–Fisher relation (McGaugh 2012), these four galaxies have similar total baryonic masses, so the differences in rotation curve shape must be due to either systematic variations in the spatial distribution of the baryons, or to varying amounts of dark matter.

The baryon distribution is at least partly responsible, since it is well documented that high surface brightness galaxies have more steeply rising rotation curves than low surface brightness systems (see e.g. McGaugh & de Blok 1998; Swaters et al. 2009, and references therein). Quantitatively, however, the differences cannot be fully ascribed to baryons (see below), so the diversity seen in Fig. 5 reflects large systematic variations in the inner dark matter content as well.

4.3 The challenge to ΛCDM

The comparison between observed and simulated rotation curves thus highlights two challenges to ΛCDM. One is to understand the
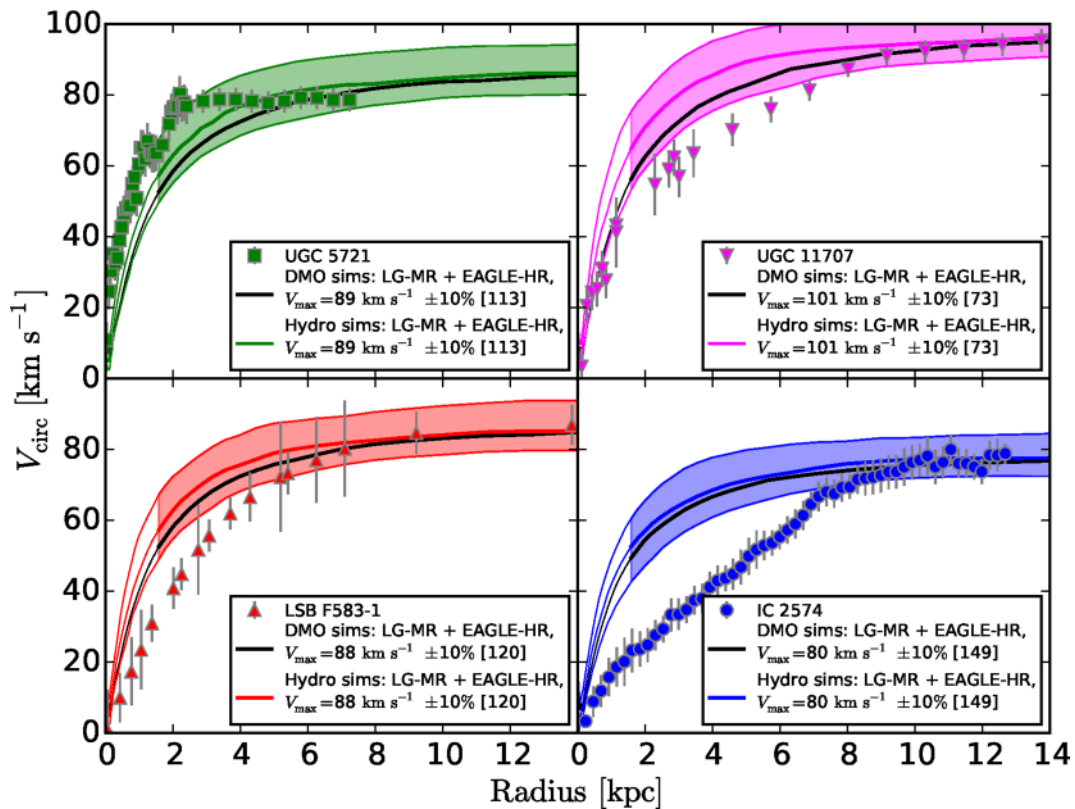
Figure 5. Rotation curves of four dwarf irregular galaxies of approximately the same maximum rotation speed ($\sim$80–100 km s^{-1}) and galaxy mass, chosen to illustrate the diversity of rotation curve shape at *given* V_{max}. As in previous figures, coloured solid curves and shaded areas correspond to the median (and 10th–90th percentile) circular velocity curve of simulated galaxies matching (within 10 per cent) the maximum circular velocity of each galaxy. Note that the observed rotation curves exhibit a much wider diversity than seen in the EAGLE and LG simulations, from galaxies like UGC 5721, which are consistent with our simulations, to galaxies like IC 2574, which show a much more slowly rising rotation curve compared with simulations, either hydrodynamical (coloured lines) or DMO (black lines).

origin of the *diversity* at fixed V_{max}, especially in dwarf galaxies, which tend to be dark-matter-dominated. These are all galaxies that form in similar haloes, have approximately the same baryonic mass, and similar morphologies. Some diversity induced by differences in the distribution of the baryonic component is expected, but clearly the observed diversity is much greater than in our simulations.

The second, and more worrying, concern is the *inner mass deficit* that some of these galaxies seem to exhibit relative to the ΛCDM simulation predictions. Indeed, except for UGC 5721, all of the galaxies shown in Fig. 5 have *less* mass in the inner 8 kpc than expected not only from our hydro simulations (shaded coloured regions) but also from a ΛCDM halo *alone* (solid black lines). Systems like UGC 11707 seem marginally consistent, and could perhaps be interpreted as outliers, but cases like IC 2574, or LSB F583-1 are too extreme to be accommodated by our model without significant change.

The mass deficit we highlight here has been noted before in the context of the 'cusp versus core' debate (see e.g. McGaugh et al. 2007, and references therein). Indeed, if constant density 'cores' were imposed on the dark matter it would be relatively straightforward to reproduce the data shown in Fig. 5. Such cores, however, would need to vary from galaxy to galaxy, *even at fixed halo mass and galaxy mass*. Indeed, a core at least as large as $\sim$5 kpc would be needed to explain the fact that the rotation curve of IC 2574 rises linearly out to $\sim$8 kpc, but ought to be much smaller in LSB F583-1 and even smaller, if at all present, in UGC 5721.

4.4 The challenge to baryon-induced core formation

The diversity of observed rotation curves presents a challenge not only to our simulations, but also to the baryon-induced 'core' creation mechanism: why would baryons carve out cores so different in galaxies that are so similar in terms of morphology, halo mass, and galaxy mass? Further, we would expect the dark matter to be most affected in systems where baryons play a more important role in the potential, such as high surface brightness galaxies, whereas observations seem to suggest the opposite trend.

A second challenge concerns the magnitude of the effect needed to create a core as large as that inferred, for example, for IC 2574. Published simulations where baryon effects create cores tend to have overall a modest effect on the total inner mass profile of the galaxy. One example is provided in Fig. 1; although baryons have carved a $\sim$1 kpc core in the dark matter halo in the simulated galaxy DG1, the total inner mass profile is actually quite similar to what is expected for galaxies of that circular velocity in our simulations (green-shaded region), which do not produce cores. This is because, to first order, the baryons that displace the dark matter to create a core take its place, leading to a modest net change in the total mass profile.

In other words, 'flattening the dark matter cusp' is not enough to explain galaxies like IC 2574. A *net removal* of large amounts of mass from the inner regions is needed to reconcile such galaxies with ΛCDM, at least if we equate the measured rotation curve with the circular velocity curve. In the case of IC 2574, at least
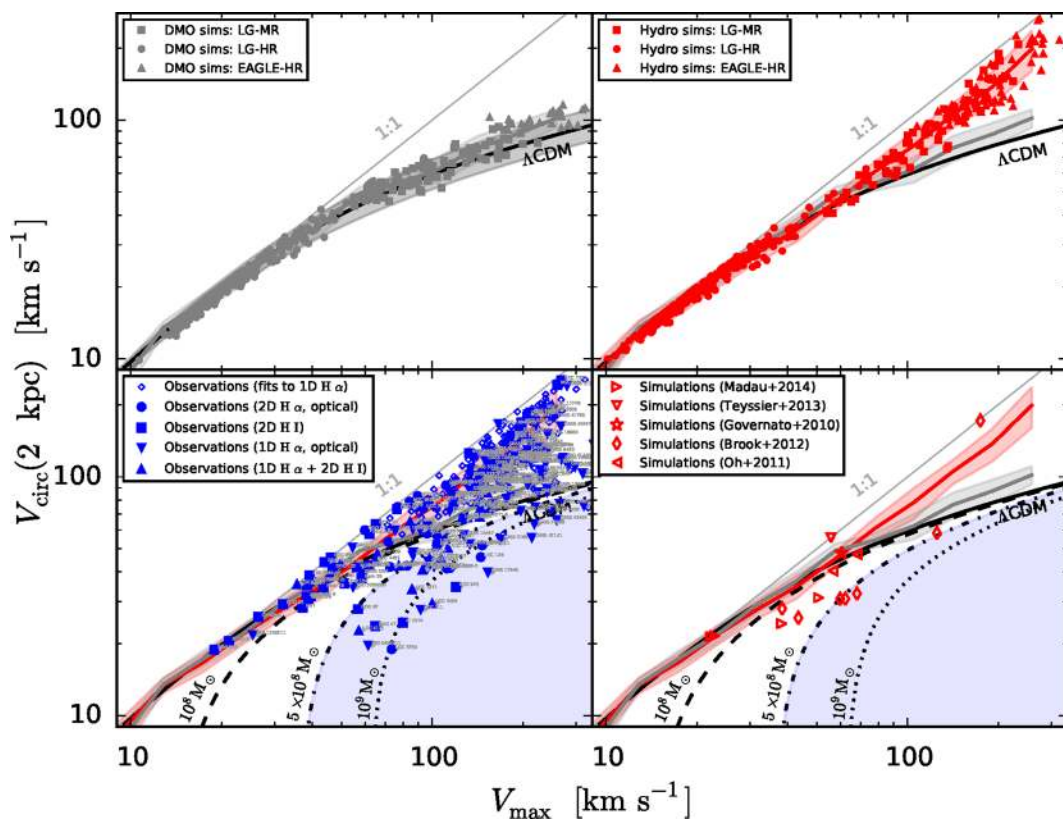
Figure 6. Circular velocity at $r = 2$ kpc versus the maximum circular velocity, V_{max}, for observed and simulated galaxies. For observed galaxies, we use the maximum rotation speed as an estimate of V_{max}, and the rotation speed measured at 2 kpc for $V_{circ}(2$ kpc$)$. We show only simulated systems for which the convergence radius is less than 2 kpc, and observed galaxies for which the nominal angular resolution of the data is better than the angle subtended by 2 kpc at the galaxy's distance. Top-left: results for DMO simulations (grey points), together with the correlation expected for NFW haloes of average concentration (solid black line). The thick grey line traces the mean $V_{circ}(2$ kpc$)$ as a function of V_{max}, whereas the shaded areas show the standard deviation. Top-right: as the top-left panel, but for simulated galaxies in the LG and EAGLE cosmological hydrodynamical simulations (red symbols). See the legend for details about each symbol type. The grey line and grey shaded region repeat the DMO correlation in the top-left panel, the red line and shaded region are analogous for the hydrodynamical simulations. Bottom-left: observed galaxies (small text labels identify individual objects). The different symbols show the different tracers observed (H I, H α, other features in the optical) and whether the observations are in 1 dimension (1D, e.g. long-slit spectroscopy) or 2 dimensions (2D, e.g. radio interferometry, integral field spectroscopy). Solid lines and shaded regions are as in the top-right panel. Note the large variation in $V_{circ}(2$ kpc$)$ at fixed V_{max} compared with the simulation results. The dotted, dashed and dot–dashed lines indicate the changes in $V_{circ}(2$ kpc$)$ induced by removing a fixed amount of mass from the inner 2 kpc of ΛCDM haloes, as labelled. The blue-shaded region highlights systems with an inner 2 kpc mass deficit exceeding 5×10^8 M$_\odot$. Bottom-right: results of recent simulations that report the formation of cores in the dark matter profiles of ΛCDM haloes. These cores lead to a slight reduction in the value of $V_{circ}(2$ kpc$)$ relative to those in our simulations, but the changes are insufficient to explain the full range of values spanned by the observational data. The dotted lines and dashed lines are as in the bottom-left panel, for ease of comparison.

$\sim 2.5 \times 10^9$ M$_\odot$ seem to have been expelled from the inner ~ 5 kpc; more than the total baryonic mass of the galaxy. It seems unlikely that baryon-induced fluctuations can cause an effect this large.

4.5 The challenge to alternative dark matter models

Finally, we note that the diversity of rotation curves illustrated in Fig. 5 disfavours solutions that rely solely on modifying the physical nature of the dark matter. Cores can indeed be produced if the dark matter is SIDM or WDM but, in this case, we would expect *all* galaxies to have cores and, in particular, galaxies of similar mass or velocity to have cores of similar size. Available simulation data are sparse but suggest that the scatter in structural properties at fixed halo mass is no larger for alternative dark matter models than for ΛCDM (e.g. Rocha et al. 2013; Lovell et al. 2014, for SIDM and WDM, respectively). This is in disagreement with rotation curve data and suggests that a mechanism unrelated to the nature of the dark matter must be invoked to explain the rotation curve shapes.

4.6 The 'inner mass deficit' problem

The prevalence of the 'inner mass deficit' problem discussed above may be characterized by comparing the inner circular velocities of observed galaxies with those of ΛCDM galaxies of matching V_{max}. We show this in Fig. 6, where we use our ΛCDM simulations, as well as the compiled rotation curve data, to plot the circular velocity at 2 kpc against the maximum measured rotation speed, V_{max}. Where data do not exist at exactly 2 kpc, we interpolate linearly between nearby data points. We choose a fixed physical radius of 2 kpc to characterize the inner mass profile because it is the minimum radius that is well resolved in all of our simulations for systems in the mass range of interest here. It is also a radius that is well resolved in all observed galaxies included in our compilation.

The grey symbols in the top-left panel of Fig. 6 show the results of our DMO simulations. The tight correlation between these quantities in the DMO case is a direct consequence of the nearly self-similar nature of ΛCDM haloes: once the cosmological parameters are specified, the circular velocity at 2 kpc may be used to predict

V_{max}, and vice versa. Variations in environment, shape and formation history result in some scatter, but overall this is quite small. For given V_{max}, the circular velocity at 2 kpc has a standard deviation of only ~0.1 dex. Our results are in good agreement with earlier DMO simulation work. The solid black line (and shaded region) in the figure indicates the expected correlation (plus 1σ scatter) for NFW haloes with the mass–concentration relation corresponding to the cosmological parameters adopted in our simulations (Ludlow et al. 2014). Note that the simulated data approach the 1:1 line for $V_{max} < 30$ km s^{-1}: this is because those haloes are intrinsically small; the radius where circular velocity profiles peak decreases steadily with decreasing circular velocity, from 4.6 to 1.9 kpc when V_{max} decreases from 30 to 15 km s^{-1}.

The inclusion of baryons modifies these correlations, as shown by the red symbols in the top-right panel of Fig. 6, which show results for our hydrodynamical simulations. The main result of including baryons is to shift the expected correlation towards higher values of $V_{circ}(2$ kpc) for galaxies with $V_{max} \gtrsim 60$ km s^{-1}. This is not surprising: the assembly of the luminous galaxy adds mass to the central few kiloparsecs and raises the circular velocity there. A tight relation between V_{max} and $V_{circ}(2$ kpc) remains; however, the scatter increases only slightly, to at most ~0.15 dex (standard deviation).

Observed galaxies are shown in the bottom-left panel of Fig. 6. The diversity of rotation curves alluded to above is clearly seen here. At $V_{max} \sim 70$ km s^{-1}, for example, the rotation speed at 2 kpc of observed galaxies spans more than a factor of ~4, or about a factor of ~16 in enclosed mass. Some of those galaxies, like DDO 168 have rotation speeds at 2 kpc comparable to the maximum ($V_{max} \sim 62$ km s^{-1}, $V_{circ}(2$ kpc$) \sim 58$ km s^{-1}), which indicates an enclosed mass of ~2.3×10^9 M$_\odot$, or about twice as much as the *total* baryonic mass of the galaxy, according to the baryonic Tully–Fisher relation; $M_{bar}/$M$_\odot = 102.3\,(V_{max}/$ km s$^{-1})^{3.82}$ (McGaugh 2012). At the other extreme, galaxies like UGC 5750 ($V_{max} \gtrsim 73$ km s^{-1})[6] have rotation speeds at 2 kpc of just ~20 km s^{-1}, corresponding to an enclosed mass of only ~2×10^8 M$_\odot$, or just about 10 per cent of its total baryonic mass.

Within their diversity, many observed galaxies actually have rotation curves that agree with ΛCDM, and fall well within the region of parameter space expected from our simulations (shown by the red-shaded area in this panel). Others do not. Galaxies *below* the solid grey line (which indicates the average DMO results in all panels) have less mass within 2 kpc than expected from a DMO simulation: if rotation velocities faithfully represent the circular velocity at this radius, then some of the central mass must have been displaced.

The dotted, dot–dashed, and dashed lines in the bottom panels of Fig. 6 quantify this effect. They indicate the result of removing a fixed amount of mass, as labelled, from the inner 2 kpc of NFW haloes on the ΛCDM correlation (solid black line). Galaxies in the light blue-shaded area below the dot–dashed curve, in particular, have a mass deficit in the inner 2 kpc of more than 5×10^8 M$_\odot$ compared with a typical ΛCDM halo. For DDO 87 ($V_{max} \gtrsim 57$ km s^{-1}, $V_{circ}(2$ kpc$) \sim 28$ km s^{-1}), for example, a galaxy that falls close to the dot–dashed line, this implies a total mass deficit in the inner 2 kpc comparable to its total baryonic mass, as estimated from the baryonic Tully–Fisher relation. Indeed, several galaxies in our compilation have apparently expelled from the inner 2 kpc a mass comparable to or larger than their total baryonic mass.

Published simulations that report baryon-induced 'cores' seem unable to match these results. We show this in the bottom-right panel of Fig. 6, where the different open symbols show the results of simulations for which the formation of a 'core' in the dark matter has been reported. A few trends seem clear. Although 'core' formation alleviates the problem in some cases by bringing down the velocities at 2 kpc, the effect is generally small; indeed, no 'cored' galaxies lie well inside the blue shaded area that characterizes systems with a mass deficit larger than 5×10^8 M$_\odot$ in the inner 2 kpc.

Further, core creation – or inner mass removal – seems ineffective in galaxies with $V_{max} > 100$ km s^{-1}. Observations, on the other hand, show sizeable 'inner mass deficits' even in galaxies with maximum rotation velocities well above 100 km s^{-1}. This may be a problem for 'baryon-induced' core formation, since it has been argued that the potential well might be too deep[7] in such systems for baryons to create a sizeable core (Brook et al. 2012). We note, however, that this conclusion is based only on two systems (see bottom-right panel of Fig. 6), and that none of those simulations include AGN feedback. It remains to be seen whether further simulation work will be able to produce inner mass deficits as large as observed in some of these massive galaxies.

With these caveats in mind, we conclude that none of the mechanisms proposed so far to explain the apparent presence of cores in dwarf galaxies has been able to fully account for their inner mass deficits and for the observed diversity of their rotation curves.

5 SUMMARY AND CONCLUSIONS

We have used circular velocity curves from recent cosmological hydrodynamical simulations of galaxy formation in a ΛCDM universe, taken from the EAGLE and LG projects, to investigate the rotation curves of galaxies and reassess the 'cusp versus core' controversy.

The circular velocity curves of simulated galaxies vary systematically as a function of their maximum circular velocity (V_{max}), but show little variation for given V_{max}. Observed rotation curves, on the other hand, show great diversity, even at fixed V_{max}, especially for dwarf galaxies. At any given maximum rotation speed, some have shapes that are consistent with the simulation predictions, others do not. Deviant galaxies typically have much lower circular velocities in the inner regions than expected in ΛCDM from the dark matter halo *alone*. This apparent inner mass deficit varies from galaxy to galaxy, even at fixed galaxy mass, and can exceed, within ~2 kpc, the total baryonic mass of a galaxy.

Although this inner mass deficit may also be interpreted as evidence for a 'core' in the dark matter profile, we argue that characterizing the problem as an inner mass deficit is more robust, since it allows simulations to be compared directly with data without relying on uncertain decomposition of the dark matter and baryonic contributions to the central mass profile, or estimating dark matter density slopes in the innermost regions, where uncertainties in observations and simulations are largest.

Models that attempt to reconcile rotation curves with ΛCDM by carving 'cores' in the dark matter through baryon-induced gravitational fluctuations offer no natural explanation for the large dispersion in the values of the observed mass deficit. Nor do they seem able, at least according to published simulations, to account quantitatively for the largest mass deficits observed.

---

[6] A rightward arrow is used in the bottom-left panel of Fig. 6 to indicate cases where the rotation curve is still rising at the outermost radius measured – the maximum observed rotation speed may therefore underestimate V_{max}.

[7] We note that Macciò et al. (2012b) report the creation of cores in more massive systems, but since these authors do not show the circular velocity profiles, we have been unable to add their results to our plot.

The diversity of observed rotation curves is also unexpected in alternative dark matter scenarios, substantially diminishing their appeal. This is because modifying the nature of dark matter may produce cores in dark haloes, but such cores would all be of similar size at given mass scale, unlike what is inferred from rotation curves.

Finally, it may be that dynamical inferences from available kinematic data need to be re-evaluated. Many of the galaxies that show the largest mass deficits (or the strongest evidence for a 'core') appear highly irregular. Complexities such as non-circular and random motions, instrumental smearing and sampling effects, and/or departures from axisymmetry and coplanarity can substantially complicate the reconstruction of circular velocity profiles from the observed kinematics. The magnitude of the effect needed to reconcile ΛCDM with the data shown in Fig. 6 seem too large, however, to be due wholly to such uncertainties.

We conclude that present rotation curve data support neither a revision of the nature of dark matter, nor current models for 'core formation' in galaxies formed in a ΛCDM universe. The mystery of the inner rotation curves of galaxies thus remains unsolved.

ACKNOWLEDGEMENTS

REFERENCES

Adams J. J., Gebhardt K., Blanc G. A., Fabricius M. H., Hill G. J., Murphy J. D., van den Bosch R. C. E., van de Ven G., 2012, ApJ, 745, 92
Adams J. J. et al., 2014, ApJ, 789, 63
Bastidas Fry A. et al., 2015, preprint (arXiv:1501.00497)
Bode P., Ostriker J. P., Turok N., 2001, ApJ, 556, 93
Brook C. B., Stinson G., Gibson B. K., Wadsley J., Quinn T., 2012, MNRAS, 424, 1275
Courteau S., 1997, AJ, 114, 2402
Crain R. A. et al., 2015, MNRAS, 450, 1937
de Blok W. J. G., Bosma A., 2002, A&A, 385, 816
de Blok W. J. G., McGaugh S. S., Rubin V. C., 2001, AJ, 122, 2396
de Blok W. J. G., Weldrake D. T. F., Walter F., 2004, in Ryder S., Pisano D., Walker M., Freeman K., eds, Proc. IAU Symp. 220, Dark Matter in Galaxies. Astron. Soc. Pac., San Francisco, p. 373
de Blok W. J. G., Walter F., Brinks E., Trachternach C., Oh S.-H., Kennicutt R. C., Jr, 2008, AJ, 136, 2648
Di Cintio A., Brook C. B., Dutton A. A., Macciò A. V., Stinson G. S., Knebe A., 2014, MNRAS, 441, 2986
Dolag K., Borgani S., Murante G., Springel V., 2009, MNRAS, 399, 497
Duffy A. R., Schaye J., Kay S. T., Dalla Vecchia C., 2008, MNRAS, 390, L64
Elbert O. D., Bullock J. S., Garrison-Kimmel S., Rocha M., Oñorbe J., Peter A. H. G., 2014, preprint (arXiv:1412.1477)
Flores R. A., Primack J. R., 1994, ApJ, 427, L1
Furlong M. et al., 2015, MNRAS, 450, 4486
Gnedin O. Y., Ostriker J. P., 2001, ApJ, 561, 61
Gnedin O. Y., Zhao H., 2002, MNRAS, 333, 299
Governato F. et al., 2010, Nature, 463, 203
Governato F. et al., 2012, MNRAS, 422, 1231
Hayashi E. et al., 2004, MNRAS, 355, 794
Hopkins P. F., 2013, MNRAS, 428, 2840
Kauffmann G., Huang M.-L., Moran S., Heckman T., 2015, MNRAS, 451, 5397
Komatsu E. et al., 2011, ApJS, 192, 18
Kuzio de Naray R., McGaugh S. S., de Blok W. J. G., 2008, ApJ, 676, 920
Lovell M. R. et al., 2012, MNRAS, 420, 2318
Lovell M. R., Frenk C. S., Eke V. R., Jenkins A., Gao L., Theuns T., 2014, MNRAS, 439, 300
Ludlow A. D., Navarro J. F., Angulo R. E., Boylan-Kolchin M., Springel V., Frenk C., White S. D. M., 2014, MNRAS, 441, 378
Macciò A. V., Dutton A. A., van den Bosch F. C., 2008, MNRAS, 391, 1940
Macciò A. V., Paduroiu S., Anderhalden D., Schneider A., Moore B., 2012a, MNRAS, 424, 1105
Macciò A. V., Stinson G., Brook C. B., Wadsley J., Couchman H. M. P., Shen S., Gibson B. K., Quinn T., 2012b, ApJ, 744, L9
Madau P., Shen S., Governato F., 2014, ApJ, 789, L17
Mashchenko S., Couchman H. M. P., Wadsley J., 2006, Nature, 442, 539
McGaugh S. S., 2012, AJ, 143, 40
McGaugh S. S., de Blok W. J. G., 1998, ApJ, 499, 41
McGaugh S. S., de Blok W. J. G., Schombert J. M., Kuzio de Naray R., Kim J. H., 2007, ApJ, 659, 149
Miralda-Escudé J., 2002, ApJ, 564, 60
Moore B., 1994, Nature, 370, 629
Navarro J. F., Eke V. R., Frenk C. S., 1996, MNRAS, 283, L72
Navarro J. F., Frenk C. S., White S. D. M., 1996, ApJ, 462, 563
Navarro J. F., Frenk C. S., White S. D. M., 1997, ApJ, 490, 493
Neto A. F. et al., 2007, MNRAS, 381, 1450
Oh S.-H., de Blok W. J. G., Brinks E., Walter F., Kennicutt R. C., Jr, 2011, AJ, 141, 193
Oh S.-H. et al., 2015, AJ, 149, 180
Oñorbe J., Boylan-Kolchin M., Bullock J. S., Hopkins P. F., Kerěs D., Faucher-Giguère C.-A., Quataert E., Murray N., 2015, preprint (arXiv:1502.02036)
Planck Collaboration XVI, 2014, A&A, 571, A16
Planck Collaboration XIII, 2015, preprint (arXiv:1502.01589)
Pontzen A., Governato F., 2014, Nature, 506, 171
Power C., Navarro J. F., Jenkins A., Frenk C. S., White S. D. M., Springel V., Stadel J., Quinn T., 2003, MNRAS, 338, 14
Prada F., Klypin A. A., Cuesta A. J., Betancort-Rijo J. E., Primack J., 2012, MNRAS, 423, 3018
Read J. I., Gilmore G., 2005, MNRAS, 356, 107
Reyes R., Mandelbaum R., Gunn J. E., Pizagno J., Lackner C. N., 2011, MNRAS, 417, 2347
Rocha M., Peter A. H. G., Bullock J. S., Kaplinghat M., Garrison-Kimmel S., Oñorbe J., Moustakas L. A., 2013, MNRAS, 430, 81
Sawala T. et al., 2014, preprint (arXiv:1412.2748)
Sawala T. et al., 2015, MNRAS, 448, 2941
Schaller M. et al., 2015, MNRAS, 451, 1247
Schaye J., 2004, ApJ, 609, 667
Schaye J. et al., 2015, MNRAS, 446, 521
Shao S., Gao L., Theuns T., Frenk C. S., 2013, MNRAS, 430, 2346
Simon J. D., Bolatto A. D., Leroy A., Blitz L., 2003, ApJ, 596, 957
Spergel D. N., Steinhardt P. J., 2000, Phys. Rev. Lett., 84, 3760
Springel V., 2005, MNRAS, 364, 1105
Springel V., White S. D. M., Tormen G., Kauffmann G., 2001, MNRAS, 328, 726
Swaters R. A., Madore B. F., van den Bosch F. C., Balcells M., 2003, ApJ, 583, 732
Swaters R. A., Sancisi R., van Albada T. S., van der Hulst J. M., 2009, A&A, 493, 871
Teyssier R., Pontzen A., Dubois Y., Read J. I., 2013, MNRAS, 429, 3068
van den Bosch F. C., Robertson B. E., Dalcanton J. J., de Blok W. J. G., 2000, AJ, 119, 1579
Viel M., Becker G. D., Bolton J. S., Haehnelt M. G., 2013, Phys. Rev. D, 88, 043502

Vogelsberger M., Zavala J., Loeb A., 2012, MNRAS, 423, 3740
Vogelsberger M. et al., 2014a, MNRAS, 444, 1518
Vogelsberger M., Zavala J., Simpson C., Jenkins A., 2014b, MNRAS, 444, 3684
Walter F., Brinks E., de Blok W. J. G., Bigiel F., Kennicutt R. C., Jr, Thornley M. D., Leroy A., 2008, AJ, 136, 2563
Zavala J., Vogelsberger M., Walker M. G., 2013, MNRAS, 431, L20
Zhao D. H., Jing Y. P., Mo H. J., Börner G., 2009, ApJ, 707, 354

APPENDIX: OBSERVED ROTATION CURVE COMPILATION

Our sample of galaxy rotation curves is drawn from several sources. We describe each set of observations in Sections A1–A10; the key properties of the individual rotation curves are summarized in Table A1.

A1 Kauffmann et al. (2015)

This publication presents 187 rotation curves for galaxies in the *GALEX* Arecibo Sloan Survey (GASS) with maximum rotation velocities of 90–350 km s^{-1}. Long-slit spectra were measured using the blue-channel spectrograph on the 6.5-m Multi Mirror Telescope and the Dual Imaging Spectrograph on the 3.5-m Apache Point Observatory telescope, with angular resolutions of 1.25 and 1.5 arcsec, respectively. Though long-slit spectroscopy offers excellent angular resolution, the main drawback is that the velocity field is measured only along one direction through the galaxy, making possible errors due to, for example, non-circular motions more difficult to quantify. For each spectrum, an attempt was made to produce two rotation curves: one derived from H α emission, and a second from fitting stellar absorption templates. The stellar absorption based rotation curves are typically in good agreement with the H α curves, but of slightly better quality, so we use these where possible. Of the 187 rotation curves in the sample, we retain 106 in our compilation, the rest being of insufficient quality, resolution or extent for use in our analysis. Of these, 99 are stellar absorption based rotation curves (of which 52 also have good H α rotation curves, which we discard) and 7 are H α based. For brevity, we omit all discarded rotation curves from this source in Table A1.

A2 Oh et al. (2015)

This publication presents 26 rotation curves for galaxies in the Local Irregulars That Trace Luminosity Extremes, The H I Nearby Galaxy Survey (LITTLE THINGS) sample. This observing programme is closely related to the THINGS survey (see Section A4). The maximum measured rotation velocities of these galaxies range from about 20 to 120 km s^{-1}. Observations were taken using the National Radio Astronomy Observatory (NRAO) Very Large Array. The angular resolution of 6 arcsec is a factor of 2 better than that of the THINGS survey. Radio interferometry leads naturally to two-dimensional velocity maps. H I observations are traditionally better than their optical (usually H α) counterparts at mapping the velocity field in the outskirts of galaxies at the cost of poorer spatial resolution throughout. The LITTLE THINGS sample offers a good compromise, with sufficient resolution to probe the inner kiloparsec. The rotation curves were constructed from the velocity fields using a tilted-ring model, with asymmetric drift corrections applied as needed. We retain all 26 galaxies in our sample.

A3 Adams et al. (2014)

This publication presents a sample of seven rotation curves of galaxies with maximum rotation velocities of about 100 km s^{-1}. The velocity fields were measured with the VIRUS-W integral field spectrograph on the 2.7-m Harlan J. Smith telescope at McDonald Observatory. The use of an integral field unit (IFU) allows measurement of the velocity field in two dimensions, while maintaining the high spatial resolution typical of optical rotation curves: the fibres feeding the spectrograph have diameters of 3.1 arcsec. The velocity field is constructed by simultaneous mapping of the H β line and two O III lines. The rotation curves were constructed from the velocity fields using a tilted-ring model. We retain all seven galaxies in our sample.

A4 de Blok et al. (2008) and Oh et al. (2011)

These two publications are part of the THINGS project. The 19 rotation curves presented in de Blok et al. (2008) are those that are most straightforwardly derived, while seven of those requiring more careful analysis were presented in Oh et al. (2011, in some cases reanalysing galaxies from de Blok et al. 2008). Maximum measured rotation velocities are 30–300 km s^{-1}. The survey was carried out with the NRAO Very Large Array in B, C and D configurations. The angular resolution of 12 arcsec is substantially better than that of most earlier H I rotation curve measurements. The rotation curves were constructed from the velocity fields using a tilted-ring model. Four galaxies from Oh et al. (2011) – Ho I, Ho II, M81dwB and DDO 53 – required substantial asymmetric drift corrections. We retain 15 of the 19 galaxies from de Blok et al. (2008), discarding three that were reanalyzed by Oh et al. (2011) and NGC 4826, which appears to have a counter-rotating disc component that complicates the interpretation. We discard Ho II (also named DDO 50), DDO 53, DDO 154 and NGC 2366 from the Oh et al. (2011) sample in favour of the higher angular resolution observations of Oh et al. (2015).

A5 Reyes et al. (2011)

This publication presents a collection of 189 rotation curves with maximum rotation velocities of 100–400 km s^{-1}. All are long-slit H α measurements, variously measured using the TWIN spectrograph on the 3.5-m telescope at Calar Alto Observatory (∼1.5 arcsec resolution), the CCDS spectrograph on the 2.4-m Hiltner telescope at the MDM Observatory (∼2 arcsec resolution), and the Dual Imaging Spectrograph on the 3.5-m telescope at Apache Point Observatory (∼1.5 arcsec resolution). We were not able to obtain the full rotation curve data set, but use instead the parameters of an arctangent model fit (Courteau 1997) to the rotation curves to estimate the rotation velocity at 2 kpc and at maximum (the asymptotic value of the model). We retain all 189 rotation curves in our sample, but use an open symbol type in Fig. 6 to visually separate these data from the other sources in our compilation for which we have full rotation curves.

A6 Kuzio de Naray et al. (2008)

This publication presents rotation curves for a selection of 17 galaxies with maximum rotation velocities of 50–100 km s^{-1}. These were measured with the DensePak IFU on the 3.5-m WIYN telescope at the Kitt Peak National Observatory. The instrument has a pixel size of 3 arcsec, and multiple slightly offset exposures of the same region were taken to improve the resolution of the rotation curves to

Table A1. Basic properties of galaxies in our sample. Galaxy names and distances are those used in the publication cited. The observation type specifies the spectral feature(s) used to construct the rotation curve. Resolutions assume the distance in column 3, based on angular resolution as quoted by the cited publication. $V_{circ}(2\,kpc)$ and V_{max} are the quantities plotted in Fig. 6. Explanation of notes: (1) stellar absorption-derived rotation curve preferred to H α-derived rotation curve (see Section A1); (2) galaxy excluded from our sample in favour of a more recent observation; (3) excluded due to a counter-rotating component in the rotation curve.

Galaxy	Reference	Distance (Mpc)	Observation type	Observation resolution (kpc)	$V_{circ}(2\,kpc)$ (km s^{-1})	V_{max} (km s^{-1})	Notes
GASS 9891	Kauffmann et al. (2015)	110.5	Stellar abs.	0.8	122.3	$\geq$353.0	(1)
GASS 9463	Kauffmann et al. (2015)	152.5	H α	1.1	127.6	$\geq$239.9	–
GASS 8096	Kauffmann et al. (2015)	147.8	Stellar abs.	0.9	122.7	$\geq$187.4	(1)
GASS 7286	Kauffmann et al. (2015)	115.2	Stellar abs.	0.7	85.3	141.2	(1)
GASS 7031	Kauffmann et al. (2015)	141.8	Stellar abs.	0.9	99.7	171.2	–
GASS 6583	Kauffmann et al. (2015)	206.9	Stellar abs.	1.2	88.3	$\geq$152.9	–
GASS 57017	Kauffmann et al. (2015)	138.3	H α	1.0	96.2	$\geq$178.0	–
GASS 56612	Kauffmann et al. (2015)	124.2	Stellar abs.	0.7	128.6	$\geq$156.6	–
GASS 52297	Kauffmann et al. (2015)	140.5	Stellar abs.	0.8	84.1	$\geq$116.5	–
GASS 51899	Kauffmann et al. (2015)	165.7	Stellar abs.	1.0	93.9	139.8	(1)
GASS 51416	Kauffmann et al. (2015)	190.6	Stellar abs.	1.1	77.8	118.3	–
GASS 51351	Kauffmann et al. (2015)	125.5	Stellar abs.	0.9	240.1	280.0	(1)
GASS 48356	Kauffmann et al. (2015)	122.9	Stellar abs.	0.9	124.4	139.0	(1)
GASS 47221	Kauffmann et al. (2015)	136.2	Stellar abs.	0.8	77.0	$\geq$140.4	(1)
GASS 42402	Kauffmann et al. (2015)	197.0	Stellar abs.	1.2	66.0	$\geq$259.1	–
GASS 42141	Kauffmann et al. (2015)	154.2	Stellar abs.	1.1	55.6	214.1	–
GASS 42140	Kauffmann et al. (2015)	195.7	Stellar abs.	1.2	89.2	$\geq$240.9	–
GASS 42025	Kauffmann et al. (2015)	157.2	Stellar abs.	0.9	86.1	$\geq$224.3	(1)
GASS 41783	Kauffmann et al. (2015)	158.9	Stellar abs.	1.1	177.4	254.3	(1)
GASS 4137	Kauffmann et al. (2015)	190.6	Stellar abs.	1.1	66.5	$\geq$127.3	–
GASS 41323	Kauffmann et al. (2015)	188.4	Stellar abs.	1.1	41.3	96.4	–
GASS 4130	Kauffmann et al. (2015)	191.9	Stellar abs.	1.4	102.8	233.8	–
GASS 4094	Kauffmann et al. (2015)	118.2	Stellar abs.	0.7	116.4	193.3	–
GASS 4057	Kauffmann et al. (2015)	170.0	Stellar abs.	1.0	138.9	$\geq$192.0	–
GASS 4048	Kauffmann et al. (2015)	177.3	Stellar abs.	1.1	100.3	$\geq$182.1	(1)
GASS 4040	Kauffmann et al. (2015)	115.2	Stellar abs.	0.7	122.7	140.6	–
GASS 4038	Kauffmann et al. (2015)	178.6	Stellar abs.	1.1	71.5	$\geq$248.4	(1)
GASS 40317	Kauffmann et al. (2015)	174.7	Stellar abs.	1.0	153.8	195.4	(1)
GASS 40257	Kauffmann et al. (2015)	168.3	Stellar abs.	1.0	75.3	$\geq$150.0	–
GASS 40247	Kauffmann et al. (2015)	167.9	Stellar abs.	1.2	162.6	267.4	–
GASS 3971	Kauffmann et al. (2015)	182.4	Stellar abs.	1.3	106.8	228.4	(1)
GASS 39595	Kauffmann et al. (2015)	186.3	Stellar abs.	1.1	182.0	$\geq$208.0	(1)
GASS 39567	Kauffmann et al. (2015)	133.6	Stellar abs.	0.8	145.4	$\geq$182.9	(1)
GASS 38964	Kauffmann et al. (2015)	137.9	Stellar abs.	1.0	110.2	297.9	(1)
GASS 38758	Kauffmann et al. (2015)	124.6	Stellar abs.	0.9	132.9	233.7	(1)
GASS 38472	Kauffmann et al. (2015)	113.1	Stellar abs.	0.7	89.7	139.1	–
GASS 3819	Kauffmann et al. (2015)	194.0	Stellar abs.	1.2	60.6	86.3	(1)
GASS 3817	Kauffmann et al. (2015)	192.7	Stellar abs.	1.2	71.8	$\geq$114.3	(1)
GASS 3777	Kauffmann et al. (2015)	169.6	Stellar abs.	1.0	107.8	$\geq$134.1	(1)
GASS 3645	Kauffmann et al. (2015)	131.5	Stellar abs.	0.8	115.2	211.9	(1)
GASS 3524	Kauffmann et al. (2015)	162.7	Stellar abs.	1.0	114.1	237.9	(1)
GASS 3524	Kauffmann et al. (2015)	162.7	H α	1.0	122.4	$\geq$199.9	–
GASS 3509	Kauffmann et al. (2015)	207.3	Stellar abs.	1.2	187.4	244.8	(1)
GASS 3439	Kauffmann et al. (2015)	165.3	Stellar abs.	1.0	113.0	158.3	–
GASS 3261	Kauffmann et al. (2015)	160.6	Stellar abs.	1.0	39.5	$\geq$58.2	–
GASS 3189	Kauffmann et al. (2015)	164.5	H α	1.0	54.7	$\geq$168.3	–
GASS 30811	Kauffmann et al. (2015)	209.4	Stellar abs.	1.3	103.4	$\geq$316.1	–
GASS 30479	Kauffmann et al. (2015)	131.9	Stellar abs.	0.8	121.1	$\geq$137.8	(1)
GASS 30338	Kauffmann et al. (2015)	179.0	Stellar abs.	1.1	134.1	$\geq$227.4	(1)
GASS 29892	Kauffmann et al. (2015)	156.7	Stellar abs.	0.9	118.1	268.5	(1)
GASS 29842	Kauffmann et al. (2015)	146.0	Stellar abs.	1.1	138.0	215.3	(1)
GASS 29555	Kauffmann et al. (2015)	135.3	Stellar abs.	0.8	44.2	$\geq$97.1	(1)
GASS 27167	Kauffmann et al. (2015)	162.7	Stellar abs.	1.0	134.6	175.1	(1)
GASS 26822	Kauffmann et al. (2015)	161.0	Stellar abs.	1.2	97.2	206.0	(1)
GASS 25214	Kauffmann et al. (2015)	133.2	Stellar abs.	0.8	46.8	86.4	–
GASS 24496	Kauffmann et al. (2015)	180.3	Stellar abs.	1.1	121.2	$\geq$198.2	(1)
GASS 24366	Kauffmann et al. (2015)	176.0	Stellar abs.	1.1	123.7	$\geq$191.7	–
GASS 24168	Kauffmann et al. (2015)	111.4	Stellar abs.	0.7	86.3	$\geq$240.5	(1)

Table A1. *– continued*

Galaxy	Reference	Distance (Mpc)	Observation type	Observation resolution (kpc)	$V_{circ}(2kpc)$ (km s^{-1})	V_{max} (km s^{-1})	Notes
GASS 24094	Kauffmann et al. (2015)	184.6	Stellar abs.	1.1	149.5	≥183.1	–
GASS 23450	Kauffmann et al. (2015)	203.9	Stellar abs.	1.2	92.9	207.5	–
GASS 23315	Kauffmann et al. (2015)	140.9	Stellar abs.	0.8	101.0	≥133.6	(1)
GASS 22999	Kauffmann et al. (2015)	194.9	Stellar abs.	1.2	63.5	≥218.1	(1)
GASS 21842	Kauffmann et al. (2015)	192.7	Stellar abs.	1.2	100.7	227.4	–
GASS 20292	Kauffmann et al. (2015)	128.1	Stellar abs.	0.8	93.7	166.6	–
GASS 20133	Kauffmann et al. (2015)	209.4	Stellar abs.	1.3	73.1	≥151.5	–
GASS 20041	Kauffmann et al. (2015)	132.3	Stellar abs.	0.8	55.4	≥109.4	(1)
GASS 18900	Kauffmann et al. (2015)	194.0	Stellar abs.	1.2	151.0	≥241.4	–
GASS 18335	Kauffmann et al. (2015)	184.6	Stellar abs.	1.1	111.5	≥281.8	–
GASS 17684	Kauffmann et al. (2015)	154.6	Stellar abs.	0.9	91.1	≥256.2	(1)
GASS 17640	Kauffmann et al. (2015)	149.5	Stellar abs.	0.9	39.8	≥153.1	–
GASS 15257	Kauffmann et al. (2015)	123.3	Stellar abs.	0.7	59.8	≥75.4	–
GASS 15181	Kauffmann et al. (2015)	200.4	Stellar abs.	1.2	74.5	≥219.8	–
GASS 14831	Kauffmann et al. (2015)	190.2	Stellar abs.	1.1	77.2	265.2	(1)
GASS 14247	Kauffmann et al. (2015)	141.3	Stellar abs.	1.0	75.8	≥318.3	–
GASS 14017	Kauffmann et al. (2015)	169.6	Stellar abs.	1.0	129.3	≥207.2	–
GASS 12460	Kauffmann et al. (2015)	211.6	Stellar abs.	1.3	136.9	≥343.4	(1)
GASS 12069	Kauffmann et al. (2015)	166.2	Stellar abs.	1.2	86.3	≥138.6	(1)
GASS 12002	Kauffmann et al. (2015)	157.2	Stellar abs.	0.9	142.7	208.3	–
GASS 11956	Kauffmann et al. (2015)	169.2	Stellar abs.	1.0	81.1	≥176.6	(1)
GASS 11845	Kauffmann et al. (2015)	155.5	Stellar abs.	1.1	95.7	167.9	(1)
GASS 11824	Kauffmann et al. (2015)	162.7	H α	1.0	72.2	≥196.7	–
GASS 11808	Kauffmann et al. (2015)	205.1	Stellar abs.	1.2	122.3	≥194.9	–
GASS 11514	Kauffmann et al. (2015)	183.3	Stellar abs.	1.1	106.0	164.9	(1)
GASS 11437	Kauffmann et al. (2015)	113.1	Stellar abs.	0.7	83.6	≥183.0	(1)
GASS 11386	Kauffmann et al. (2015)	197.9	Stellar abs.	1.2	96.3	148.1	–
GASS 11349	Kauffmann et al. (2015)	109.6	Stellar abs.	0.7	98.5	≥144.0	(1)
GASS 11270	Kauffmann et al. (2015)	169.2	H α	1.0	50.6	54.5	–
GASS 11223	Kauffmann et al. (2015)	152.0	Stellar abs.	1.1	117.5	≥184.3	–
GASS 11120	Kauffmann et al. (2015)	116.1	Stellar abs.	0.8	165.7	≥197.8	(1)
GASS 11087	Kauffmann et al. (2015)	161.0	Stellar abs.	1.0	116.1	191.8	(1)
GASS 11019	Kauffmann et al. (2015)	154.2	Stellar abs.	0.9	87.6	≥133.4	(1)
GASS 10949	Kauffmann et al. (2015)	112.2	Stellar abs.	0.7	94.1	144.1	–
GASS 10948	Kauffmann et al. (2015)	110.5	Stellar abs.	0.7	96.2	≥142.5	(1)
GASS 10943	Kauffmann et al. (2015)	117.8	Stellar abs.	0.7	105.7	152.3	(1)
GASS 10942	Kauffmann et al. (2015)	107.5	Stellar abs.	0.6	42.0	≥101.4	–
GASS 10884	Kauffmann et al. (2015)	110.1	Stellar abs.	0.7	93.6	171.1	(1)
GASS 10850	Kauffmann et al. (2015)	152.0	Stellar abs.	0.9	114.2	≥204.7	(1)
GASS 10841	Kauffmann et al. (2015)	115.6	Stellar abs.	0.7	165.9	166.0	–
GASS 10831	Kauffmann et al. (2015)	116.9	H α	0.7	127.1	158.9	–
GASS 10827	Kauffmann et al. (2015)	128.9	Stellar abs.	0.8	108.5	≥166.2	–
GASS 10813	Kauffmann et al. (2015)	114.8	Stellar abs.	0.7	117.6	149.5	–
GASS 10447	Kauffmann et al. (2015)	201.7	Stellar abs.	1.2	57.1	≥127.2	–
GASS 10404	Kauffmann et al. (2015)	154.6	Stellar abs.	0.9	110.2	≥166.0	–
GASS 10358	Kauffmann et al. (2015)	158.5	Stellar abs.	1.0	52.2	≥133.3	–
GASS 10218	Kauffmann et al. (2015)	198.7	Stellar abs.	1.2	81.2	≥117.5	(1)
GASS 10019	Kauffmann et al. (2015)	131.9	Stellar abs.	0.8	117.2	≥177.2	(1)
WLM	Oh et al. (2015)	1.0	H I	<0.1	35.1	38.5	–
UGC 8508	Oh et al. (2015)	2.6	H I	0.1	46.1	≥46.1	–
NGC 3738	Oh et al. (2015)	4.9	H I	0.1	125.6	≥132.7	–
NGC 2366	Oh et al. (2015)	3.4	H I	0.1	41.9	59.8	–
NGC 1569	Oh et al. (2015)	3.4	H I	0.1	36.6	39.3	–
LSB F564-V3	Oh et al. (2015)	8.7	H I	0.3	38.7	39.2	–
IC 1613	Oh et al. (2015)	0.7	H I	<0.1	20.5	21.1	–
IC 10	Oh et al. (2015)	0.7	H I	<0.1	–	≥36.4	–
Haro 36	Oh et al. (2015)	9.3	H I	0.3	37.6	≥58.2	–
Haro 29	Oh et al. (2015)	5.9	H I	0.2	34.4	43.5	–
DDO 87	Oh et al. (2015)	7.7	H I	0.2	28.0	≥56.6	–
DDO 70	Oh et al. (2015)	1.3	H I	<0.1	43.9	≥43.9	–
DDO 53	Oh et al. (2015)	3.6	H I	0.1	29.2	≥32.0	–
DDO 52	Oh et al. (2015)	10.3	H I	0.3	42.6	≥61.7	–
DDO 50	Oh et al. (2015)	3.4	H I	0.1	31.2	38.8	–

Table A1. – *continued*

Galaxy	Reference	Distance (Mpc)	Observation type	Observation resolution (kpc)	V_{circ}(2kpc) (km s^{-1})	V_{max} (km s^{-1})	Notes
DDO 47	Oh et al. (2015)	5.2	H I	0.1	23.7	≥64.7	–
DDO 46	Oh et al. (2015)	6.1	H I	0.2	73.2	76.3	–
DDO 43	Oh et al. (2015)	7.8	H I	0.2	31.5	≥38.3	–
DDO 216	Oh et al. (2015)	1.1	H I	<0.1	18.9	≥18.9	–
DDO 210	Oh et al. (2015)	0.9	H I	<0.1	–	≥12.0	–
DDO 168	Oh et al. (2015)	4.3	H I	0.1	57.5	61.9	–
DDO 154	Oh et al. (2015)	3.7	H I	0.1	35.8	≥51.1	–
DDO 133	Oh et al. (2015)	3.5	H I	0.1	41.6	46.7	–
DDO 126	Oh et al. (2015)	4.9	H I	0.1	30.7	38.7	–
DDO 101	Oh et al. (2015)	6.4	H I	0.2	63.3	≥64.9	–
CVnIdwA	Oh et al. (2015)	3.6	H I	0.1	25.9	26.4	–
UGC 2259	Adams et al. (2014)	9.9	H β +O III	0.1	74.0	≥93.4	–
UGC 11707	Adams et al. (2014)	15.0	H β +O III	0.2	51.6	≥103.7	–
NGC 959	Adams et al. (2014)	9.9	H β +O III	0.1	78.6	≥84.1	–
NGC 5949	Adams et al. (2014)	14.3	H β +O III	0.2	92.2	≥111.2	–
NGC 5204	Adams et al. (2014)	3.2	H β +O III	<0.1	83.2	≥89.4	–
NGC 2976	Adams et al. (2014)	3.6	H β +O III	0.1	74.8	≥76.8	–
NGC 2552	Adams et al. (2014)	11.4	H β +O III	0.2	57.9	≥96.1	–
NGC 2366	Oh et al. (2011)	3.4	H I	0.2	43.2	≥66.7	(2)
M81 dw B	Oh et al. (2011)	5.3	H I	0.3	31.6	≥39.5	–
IC 2574	Oh et al. (2011)	4.0	H I	0.2	24.5	80.0	–
Ho II	Oh et al. (2011)	3.4	H I	0.2	27.9	37.5	(2)
Ho I	Oh et al. (2011)	3.8	H I	0.2	28.3	37.2	–
DDO 53	Oh et al. (2011)	3.6	H I	0.2	32.4	32.5	(2)
DDO 154	Oh et al. (2011)	4.3	H I	0.2	34.5	≥50.0	(2)
UGC 5750	Kuzio de Naray et al. (2008)	56.1	H α	0.5	19.0	≥73.4	–
UGC 477	Kuzio de Naray et al. (2008)	35.5	H α	0.3	41.3	≥111.7	–
UGC 4325	Kuzio de Naray et al. (2008)	10.1	H α	0.1	82.4	≥110.7	(2)
UGC 191	Kuzio de Naray et al. (2008)	17.6	H α	0.2	78.0	≥97.2	–
UGC 1551	Kuzio de Naray et al. (2008)	20.2	H α	0.2	42.4	≥82.5	–
UGC 1281	Kuzio de Naray et al. (2008)	5.5	H α	0.1	37.8	≥45.8	–
UGC 128	Kuzio de Naray et al. (2008)	60.0	H α	0.6	46.1	144.9	–
UGC 11820	Kuzio de Naray et al. (2008)	13.3	H α	0.1	80.1	96.9	–
NGC 959	Kuzio de Naray et al. (2008)	7.8	H α	0.1	76.7	79.2	(2)
NGC 7137	Kuzio de Naray et al. (2008)	22.5	H α	0.2	53.4	≥71.6	–
NGC 4395	Kuzio de Naray et al. (2008)	3.5	H α	<0.1	–	≥32.7	–
LSB F583-4	Kuzio de Naray et al. (2008)	49.0	H α	0.5	42.1	≥95.8	–
LSB F583-1	Kuzio de Naray et al. (2008)	32.0	H α	0.3	42.0	≥72.4	–
LSB F568-3	Kuzio de Naray et al. (2008)	77.0	H α	0.7	41.4	≥114.3	–
LSB F563-V2	Kuzio de Naray et al. (2008)	61.0	H α	0.6	52.9	≥103.8	–
LSB F563-1	Kuzio de Naray et al. (2008)	45.0	H α	0.4	51.7	≥146.4	–
DDO 64	Kuzio de Naray et al. (2008)	6.1	H α	0.1	59.8	≥59.8	–
NGC 925	de Blok et al. (2008)	9.2	H I	0.5	34.7	≥119.9	–
NGC 7793	de Blok et al. (2008)	3.9	H I	0.2	76.2	117.9	–
NGC 7331	de Blok et al. (2008)	14.7	H I	0.8	253.2	268.1	–
NGC 6946	de Blok et al. (2008)	5.9	H I	0.3	132.5	224.3	–
NGC 5055	de Blok et al. (2008)	10.1	H I	0.6	185.3	211.6	–
NGC 4826	de Blok et al. (2008)	7.5	H I	0.4	−166.7	180.2	(3)
NGC 4736	de Blok et al. (2008)	4.7	H I	0.3	168.7	198.3	–
NGC 3627	de Blok et al. (2008)	9.3	H I	0.5	178.0	207.1	–
NGC 3621	de Blok et al. (2008)	6.6	H I	0.4	102.9	≥159.2	–
NGC 3521	de Blok et al. (2008)	10.7	H I	0.6	192.1	233.4	–
NGC 3198	de Blok et al. (2008)	13.8	H I	0.8	76.7	158.7	–
NGC 3031	de Blok et al. (2008)	3.6	H I	0.2	242.2	259.8	–
NGC 2976	de Blok et al. (2008)	3.6	H I	0.2	75.0	≥86.2	(2)
NGC 2903	de Blok et al. (2008)	8.9	H I	0.5	120.1	215.5	–
NGC 2841	de Blok et al. (2008)	14.1	H I	0.8	–	323.9	–
NGC 2403	de Blok et al. (2008)	3.2	H I	0.2	97.4	143.9	–
NGC 2366	de Blok et al. (2008)	3.4	H I	0.2	43.2	≥66.7	(2)
IC 2574	de Blok et al. (2008)	4.0	H I	0.2	20.6	≥78.5	(2)
DDO 154	de Blok et al. (2008)	4.3	H I	0.2	34.5	≥50.0	(2)
NGC 6822	de Blok, Weldrake & Walter (2004)	0.5	H I	<0.1	41.8	≥56.3	–
UGC 8490	Swaters et al. (2003)	20.5	H I + H α	0.1	30.0	80.1	(2)
UGC 731	Swaters et al. (2003)	8.0	H I + H α	<0.1	61.5	≥74.0	(3)

Table A1. – *continued*

Galaxy	Reference	Distance (Mpc)	Observation type	Observation resolution (kpc)	$V_{circ}(2\text{kpc})$ (km s^{-1})	V_{max} (km s^{-1})	Notes
UGC 5721	Swaters et al. (2003)	6.7	H I + H α	<0.1	76.2	80.4	(2)
UGC 4499	Swaters et al. (2003)	13.0	H I + H α	0.1	46.2	≥74.2	(2)
UGC 4325	Swaters et al. (2003)	10.1	H I + H α	0.1	77.0	104.6	(2)
UGC 2259	Swaters et al. (2003)	9.8	H I + H α	0.1	78.8	93.7	(2)
UGC 12732	Swaters et al. (2003)	13.2	H I + H α	0.1	45.8	≥98.0	–
UGC 11861	Swaters et al. (2003)	25.1	H I + H α	0.1	80.4	164.0	(2)
UGC 11707	Swaters et al. (2003)	15.9	H I + H α	0.1	51.3	≥99.9	(2)
UGC 11557	Swaters et al. (2003)	23.8	H I + H α	0.1	35.1	≥84.5	(2)
LSB F574-1	Swaters et al. (2003)	96.0	H I + H α	0.5	57.9	≥104.2	–
LSB F568-V1	Swaters et al. (2003)	80.0	H I + H α	0.4	67.0	124.9	–
LSB F568-3	Swaters et al. (2003)	77.0	H I + H α	0.4	32.5	111.2	(2)
LSB F568-1	Swaters et al. (2003)	85.0	H I + H α	0.4	67.9	≥130.7	–
LSB F563-V2	Swaters et al. (2003)	61.0	H I + H α	0.3	87.7	≥113.1	(2)
UGC 711	de Blok & Bosma (2002)	26.4	H α	0.3	27.8	≥91.6	–
UGC 5750	de Blok & Bosma (2002)	56.0	H I + H α	0.5	20.0	≥49.6	(2)
UGC 5005	de Blok & Bosma (2002)	52.0	H I + H α	0.5	29.6	≥100.0	–
UGC 4325	de Blok & Bosma (2002)	10.1	H I + H α	0.1	73.8	≥122.6	(2)
UGC 4173	de Blok & Bosma (2002)	16.8	H I + H α	0.2	22.8	≥57.0	–
UGC 3371	de Blok & Bosma (2002)	12.8	H I + H α	0.1	33.9	≥85.7	–
UGC 3137	de Blok & Bosma (2002)	18.4	H I + H α	0.2	45.6	106.9	–
UGC 1281	de Blok & Bosma (2002)	5.5	H I + H α	0.1	37.7	≥56.9	(2)
UGC 1230	de Blok & Bosma (2002)	51.0	H I + H α	0.5	50.5	112.7	–
UGC 10310	de Blok & Bosma (2002)	15.6	H I + H α	0.1	38.9	≥75.0	(2)
NGC 5023	de Blok & Bosma (2002)	4.8	H I + H α	<0.1	64.9	≥84.4	–
NGC 4455	de Blok & Bosma (2002)	6.8	H I + H α	0.1	44.9	≥64.4	–
NGC 4395	de Blok & Bosma (2002)	3.5	H I + H α	<0.1	57.0	≥84.2	(2)
NGC 3274	de Blok & Bosma (2002)	6.7	H I + H α	0.1	82.5	82.6	(2)
NGC 2366	de Blok & Bosma (2002)	3.4	H I + H α	<0.1	54.0	55.5	(2)
NGC 1560	de Blok & Bosma (2002)	3.0	H I + H α	<0.1	42.6	≥77.5	–
NGC 100	de Blok & Bosma (2002)	11.2	H α	0.1	60.0	≥91.2	–
LSB F563-1	de Blok & Bosma (2002)	45.0	H I + H α	0.4	57.1	≥114.1	(2)
IC 2233	de Blok & Bosma (2002)	10.5	H I + H α	0.1	40.8	≥92.8	–
DDO 64	de Blok & Bosma (2002)	6.1	H I + H α	0.1	46.3	≥46.9	(2)
DDO 52	de Blok & Bosma (2002)	5.3	H I + H α	0.1	43.1	≥50.0	(2)
DDO 47	de Blok & Bosma (2002)	4.0	H I + H α	<0.1	44.0	≥67.0	(2)
DDO 189	de Blok & Bosma (2002)	12.6	H I + H α	0.1	47.6	≥65.7	–
DDO 185	de Blok & Bosma (2002)	5.1	H I + H α	<0.1	43.3	≥49.6	–
UGC 6614	de Blok, McGaugh & Rubin (2001)	85.0	H α	0.6	120.2	≥205.2	–
UGC 5750	de Blok et al. (2001)	56.0	H α	0.4	23.2	≥78.9	(2)
UGC 4115	de Blok et al. (2001)	3.2	H I + H α	<0.1	–	≥39.8	–
UGC 11819	de Blok et al. (2001)	60.0	H I + H α	0.4	73.0	≥154.7	–
UGC 11748	de Blok et al. (2001)	73.0	H I + H α	0.5	198.9	250.0	–
UGC 11648	de Blok et al. (2001)	48.0	H I + H α	0.3	74.3	≥144.6	–
UGC 11616	de Blok et al. (2001)	73.0	H I + H α	0.5	87.8	≥142.8	–
UGC 11583	de Blok et al. (2001)	5.0	H I + H α	<0.1	35.6	≥35.6	–
UGC 11557	de Blok et al. (2001)	22.0	H I + H α	0.2	34.5	≥80.4	(2)
UGC 11454	de Blok et al. (2001)	91.0	H I + H α	0.7	85.8	≥152.2	–
LSB F730-V1	de Blok et al. (2001)	144.0	H α	1.0	87.3	≥145.3	–
LSB F583-4	de Blok et al. (2001)	49.0	H I + H α	0.4	44.5	≥69.9	(2)
LSB F583-1	de Blok et al. (2001)	32.0	H I + H α	0.2	40.7	≥86.9	(2)
LSB F579-V1	de Blok et al. (2001)	85.0	H I + H α	0.6	93.5	≥114.4	–
LSB F571-8	de Blok et al. (2001)	48.0	H I + H α	0.3	68.1	≥143.9	–
LSB F568-3	de Blok et al. (2001)	77.0	H I + H α	0.6	41.0	≥101.1	(2)
LSB F563-1	de Blok et al. (2001)	23.6	H I + H α	0.2	84.0	112.4	(2)
ESO 4880490	de Blok et al. (2001)	22.0	H α	0.2	62.3	≥97.1	–
ESO 4250180	de Blok et al. (2001)	86.0	H α	0.6	–	≥144.5	–
ESO 3050090	de Blok et al. (2001)	11.0	H α	0.1	34.6	≥54.6	–
ESO 3020120	de Blok et al. (2001)	69.0	H α	0.5	48.3	≥86.3	–
ESO 2060140	de Blok et al. (2001)	60.0	H α	0.4	83.6	≥118.0	–
ESO 1870510	de Blok et al. (2001)	18.0	H α	0.1	36.3	≥39.9	–
ESO 1200211	de Blok et al. (2001)	15.0	H α	0.1	21.8	≥25.4	–
ESO 0840411	de Blok et al. (2001)	80.0	H α	0.6	19.7	≥61.3	–
ESO 0140040	de Blok et al. (2001)	212.0	H α	1.5	120.3	≥272.7	–

~2 arcsec. The rotation curves were constructed from the velocity fields using a tilted-ring model. No correction for asymmetric drift was applied as the correction is expected to be <2 km s^{-1} in all cases. We retain 15 galaxies in our sample, discarding UGC 4325 (alternate name NGC 2552) and NGC 959 in favour of more recent observations.

A7 de Blok et al. (2004)

This publication presents a single, very high resolution rotation curve. Discounting the satellites of the Milky Way, NGC 6822 is the nearest late-type dwarf galaxy to us, at a distance of less than 500 kpc. This allows for a high spatial resolution (~20 pc) H I map even with the modest 8 arcsec angular resolution of the Australia Telescope Compact Array.

A8 Swaters et al. (2003)

This publication presents 15 rotation curves with maximum measured rotation velocities of about 100–150 km s^{-1}. The double spectrograph on the 200-inch Hale telescope at Mount Palomar Observatory was used to obtain long-slit H α spectra along the major axis of each galaxy. The spectra have a nominal resolution of 0.5 arcsec but, in practice, are limited by seeing of ~1–2 arcsec. The galaxies targetted also had existing H I maps, which were used to extend the H α curves to larger radii. We retain four galaxies in our sample, discarding UGC 731 that has a counter-rotating component, and UGC 8490, UGC 5721, UGC 4499, UGC 4325, UGC 2259, UGC 11861, UGC 11707, UGC 11557, LSB F568-3 and LSB F563-V2 in favour of more recent observations of the same galaxies.

A9 de Blok & Bosma (2002)

This publication presents 24 rotation curves of galaxies with maximum measured rotation velocities of about 50–100 km s^{-1}. Long-slit H α spectra were measured using the Carelec spectrograph on the 192-cm telescope at the Observatoire de Haute Provence. The angular resolution is seeing-limited to ~2 arcsec. These data are supplemented with lower resolution H I velocity maps for all but two of the galaxies, allowing the extension of the rotation curves to larger radii. We exclude UGC 5750, UGC 4325, UGC 1281, UGC 10310, NGC 4395, NGC 3274, NGC 2366, LSB F563-1 and DDO 64 from our sample in favour of more recent observations, retaining 15 galaxies.

A10 de Blok et al. (2001)

This paper presents 26 rotation curves of galaxies with maximum measured rotation velocities between 40 and 200 km s^{-1}. The 4-m Kitt Peak and 100-in Las Campanas telescopes were used to obtain long-slit H α spectra. The resolution is seeing-limited to ~1.5 arcsec. Where available, H I velocity maps supplement the H α data, extending the rotation curves to larger radii. We exclude UGC 5750, UGC 11557, LSB F583-4, LSB F583-1, LSB F568-3 and LSB F563-1 from our sample in favour of more recent observations, retaining 20 rotation curves.

This paper has been typeset from a TEX/LATEX file prepared by the author.